JAMES | Journal of Advances in Modeling Earth Systems

RESEARCH ARTICLE
10.1029/2023MS003696

Simulating Sea-Ice Deformation in Viscous-Plastic Sea-Ice Models With CD-Grids

C. Mehlmann[1], G. Capodaglio[2], and S. Danilov[3,4]

[1]Otto-von-Guericke Universität, Magdeburg, Germany, [2]Los Alamos National Laboratory, Computational Physics and Methods Group, Los Alamos, NM, USA, [3]Alfred Wegener Institute, Helmholtz Centre for Polar and Marine Research, Bremerhaven, Germany, [4]Jacobs University, Bremen, Germany

Key Points:

- The type of spatial discretization used in CD-grid approximations is important for the amount of simulated local kinematic features (LKFs)
- The CD-grid discretization based on nonconforming finite elements simulates the highest amount of LKFs
- The CD-grids resolve more LKFs than A-grids, B-grids, or C-grids

Correspondence to:

C. Mehlmann,
carolin.mehlmann@ovgu.de

Citation:

Mehlmann, C., Capodaglio, G., & Danilov, S. (2023). Simulating sea-ice deformation in viscous-plastic sea-ice models with CD-grids. *Journal of Advances in Modeling Earth Systems*, *15*, e2023MS003696. https://doi.org/10.1029/2023MS003696

Received 3 MAR 2023
Accepted 7 AUG 2023

Abstract Linear kinematic features (LKFs) are found everywhere in the Arctic sea-ice cover. They are strongly localized deformations often associated with the formation of leads and pressure ridges. In viscous-plastic (VP) sea-ice models, the simulation of LKFs depends on several factors such as the grid resolution, the numerical solver convergence, and the placement of the variables on the mesh. In this study, we compare two recently proposed discretization with a CD-grid placement with respect to their ability to reproduce LKFs. The first (CD1) is based on a nonconforming finite element discretization, whereas the second (CD2) uses a conforming subgrid discretization. To analyze their resolution properties, we evaluate runs from different models (e.g., FESOM, MPAS) on a benchmark problem using quadrilateral, hexagonal and triangular meshes. Our findings show that the CD1 setup simulates more deformation structure than the CD2 setup. This highlights the importance of the type of spatial discretization for the simulation of LKFs. Due to the higher number of degrees of freedom, both CD-grids resolve more LKFs than traditional A, B, and C-grids at fixed mesh level. This is an advantage of the CD-grid approach, as high spatial mesh resolution is needed in VP sea-ice models to simulate LKFs.

Plain Language Summary Sea ice in the polar regions is an important component of the climate system. Satellite images demonstrate that the sea-ice cover can contain long features, such as cracks or leads and areas of increased sea-ice density known as pressure ridges. In order to simulate these features, mathematical equations that describe the drift of ice are solved on a computational grid. A recent study showed that the simulation of these features on a grid with a given spacing is influenced by the way the variables are placed on grid cells. Locating them at the edge midpoints of the cells leads to simulations with more features than placing the variables on vertices or centers of cells. In this contribution, we show that, along with the placement, also the mathematical method used to approximate the equations on the computational grid plays a pivotal role on the number of simulated features.

1. Introduction

Sea ice plays a crucial role in the climate system acting as a buffer between the ocean and the atmosphere, influencing the exchange of heat, moisture and momentum (Stroeve & Notz, 2018). Linear kinematic features (LKFs), such as leads and ridges, are build in response to wind and ocean forcing. These LKFs are important indicators of sea-ice deformation, which are closely linked to the mechanical properties of sea ice (Kwok, 2001). However, simulating these features in sea-ice models has proven to be a significant challenge (Hutter et al., 2022).

In most climate models, sea ice is characterized as a viscous-plastic (VP) two dimensional continuum, which is represented either in the classical VP formulation (Hibler, 1979) or by the elastic-viscous-plastic (EVP) modification (Hunke & Dukowicz, 1997). The VP sea-ice model has been criticized in the last years for using assumptions that have no observational evidence (Coon et al., 2007; Feltham, 2008; Rampal et al., 2008), and alternative rheologies have been proposed (Dansereau et al., 2016; Rampal et al., 2016; Tsamados et al., 2013). Even so, most practical applications are still using the (E)VP formulation and will continue to apply it in the foreseeable future (Blockley et al., 2020).

It has been demonstrated in different studies that (E)VP models are able to simulate aspects of observed LKFs (Hutter & Losch, 2020). Once the resolution is high enough, these models are able to reproduce observed deformations and spatial-temporal scaling laws (Bouchat & Tremblay, 2017; Bouchat et al., 2022). The simulated LKFs however depend on numerical details used in the model realization such as the numerical solver convergence

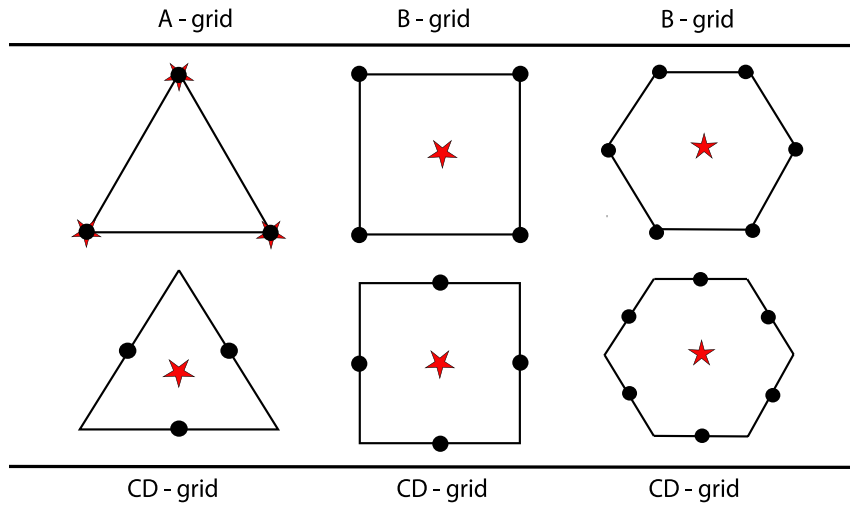

Figure 1. Variable placements (A-grid, B-grid, and CD-grid) considered in this work for several mesh cell geometries. We indicate the placement of the latitude/zonal velocity $\mathbf{v} = (u, v)$ and the staggering of the tracers by $\bullet$, and $\star$, respectively. Please note that a C-grid has the same staggering as the CD-grid with the difference that in case of a C-grid the velocity is represented by the normal component only.

(Koldunov et al., 2019; Lemieux et al., 2012), the pressure parameterization (Hutchings et al., 2005), the mesh resolution (Wang et al., 2016) or the placement of the sea-ice variables on the grid (Mehlmann et al., 2021b).

In the context of the VP sea-ice model, an increase of the mesh resolution leads to a larger amount of simulated deformation. However, increasing the spatial resolution may not always be possible in practical applications, and more elaborated spatial discretizations can be an efficient alternative. Mehlmann et al. (2021b) found that a CD-grid type discretization on quadrilateral meshes resolves more deformation than approaches which represent the velocity by its normal component at the edge midpoint (C-grids) or setups with velocities located on vertices (A-grids, B-grids). See Figure 1 for a summary of these different grid placements. The study also analyzed the simulated deformation on triangular meshes and found that the triangular CD-grid setup resolves more LKFs than the triangular A-grid. The higher amount of LKFs produced with the CD-grid can mainly be attributed to the higher number of degrees of freedom (dof). Additionally, the authors found that the quadrilateral CD-grid approach simulates a similar amount of deformation structure than quadrilateral B-grid and C-grid discretization, but on a grid twice as coarse (less velocity degrees of freedom). The same is true for the triangular CD-grid compared to the triangular A-grid.

A new CD-grid formulation has been proposed by Capodaglio et al. (2023). The approach applies a subgrid discretization based on Wachpress functions (Dasgupta, 2003) or piecewise linear basis functions (PWL) (Bailey et al., 2008). We will refer to this CD-grid discretization as CD2. The CD2 formulation differs from the CD-grid approximation used by Mehlmann et al. (2021b) in the spatial discretization of strain rates and stresses. The latter is based on a nonconforming finite element discretization (Crouzeix-Raviart element), and will be referred to as CD1 in the remainder of the paper. The question arises on how the resolution properties of CD2 approaches compare to those of CD1 and traditional A-grids, B-grids and C-grids. Answering this question is the aim of this work.

To do so, we performed a numerical analysis on a benchmark problem introduced in Mehlmann et al. (2021b), to find that in addition to the edge placement used in the CD-grid approaches, the spatial discretization also plays a crucial role for the amount of simulated deformation. This holds true for different types of grids, including quadrilateral, triangular, and hexagonal meshes. The CD2 simulations on quadrilateral and hexagonal grids are obtained with the sea-ice module of the *Model for Prediction Across Scales* (MPAS-Seaice, Capodaglio et al., 2023; Turner et al., 2021). In case of triangular meshes, we compute the CD2 approximation with the *Finite-Volume Sea Ice–Ocean model* (FESOM, Danilov et al., 2015). Please note that the CD2 discretization in FESOM (Danilov et al., 2023a) is inspired by the development of Capodaglio et al. (2023) and differs in numerical details in the subgrid discretization.

Table 1
Overview of the Model Configuration

Model	Grid	Staggering	Strain rates discretization	Solver	Transport	No. cells (2 km)	Dof
FESOM	△	A	Conforming linear FE	mEVP	FEM-FCT	151,630	N
	△	CD	Nonconforming linear FE	mEVP	Upwind	151,630	3N
	△	CD	Subgrid conforming linear FE	mEVP	FEM-FCT	151,630	3N
ICON	△	CD	Conforming linear FE	mEVP	Upwind	149,938	3N
MPAS	⬡	B	Subgrid piecewise linear basis	EVP	Remapping	74,676	4N
	⬡	CD	Subgrid piecewise linear basis	EVP	Remapping	74,676	6N
	□	B	Subgrid piecewise linear basis	EVP	Remapping	65,536	2N
	□	CD	Subgrid piecewise linear basis	EVP	Remapping	65,536	4N
CICE	□	B	Subgrid bi-linear basis	Picard	Remapping	65,536	2N
Gascoigne	□	B	Conforming linear FE	Newton	Upwind	65,536	2N
	□	CD	Nonconforming linear FE	Newton	Upwind	65,536	4N
MITgcm	□	C	Central differences	Newton	FV with flux limiter	65,536	2N

Note. The number of degrees of freedom (dof) is given per N cells.

The CD2 simulations are compared to runs conducted with the *Los Alamos Sea Ice Model* (CICE, Hunke et al., 2015), the sea-ice module of the *Icosahedral Nonhydrostatic Weather and Climate Model* (ICON, Mehlmann & Korn, 2021), the sea-ice module of the *Massachusetts Institute of Technology general circulation model* (MITgcm, Losch et al., 2010), and the setup realized in the academic software library *Gascoigne* (Becker et al., 2019). The different model setups are reported in Table 1 for ease of reference, whereas a detailed description of the model configuration is provided in Section 3.3. The paper is structured as follows. Section 2 introduces the sea-ice model equations, while Section 3 outlines the model configuration and methods applied for the analysis. Section 4 presents a numerical evaluation of the data, and a discussion is given in Section 5. The paper ends with a conclusion in Section 6.

2. Model Equations

We consider a simplified sea-ice model, where sea-ice is characterized by three variables: sea-ice velocity $\mathbf{v}$, sea-ice thickness H and sea-ice concentration A. The sea-ice dynamics is described by the following system of equations

$$m\partial_t \mathbf{v} + f_c \boldsymbol{e}_z \times \mathbf{v} = \operatorname{div} \boldsymbol{\sigma} + F, \tag{1}$$

$$\partial_t A + \operatorname{div}(\mathbf{v}A) = 0, \quad A \leq 1, \tag{2}$$

$$\partial_t H + \operatorname{div}(\mathbf{v}H) = 0, \tag{3}$$

where $m = \rho_{\text{ice}} H$ is the ice mass per unit area, $\rho_{\text{ice}} = 900\ \text{kg/m}^3$ is the density, $f_c = 1.46 \cdot 10^{-4}\text{s}^{-1}$ is the Coriolis parameter, $\boldsymbol{e}_z$ is the vertical (z-direction) unit vector, and $\boldsymbol{\sigma}$ is the internal stress. The external forces are collected in

$$F = A\,\boldsymbol{\tau}(\mathbf{v}) - \rho_{\text{ice}} H g \nabla \tilde{H}_g,$$

where g is the gravitational acceleration, $\tilde{H}_g$ is the sea surface height and $\boldsymbol{\tau}(\mathbf{v})$ describes the oceanic and atmospheric stresses. The internal stresses $\boldsymbol{\sigma}$ are related to the strain rates

$$\dot{\boldsymbol{\epsilon}} = \frac{1}{2}\left(\nabla \mathbf{v} + \nabla \mathbf{v}^T\right) \tag{4}$$

by the VP material law (Hibler, 1979)

$$\boldsymbol{\sigma} = 2\eta\dot{\boldsymbol{\epsilon}} + (\zeta - \eta)\operatorname{tr}(\dot{\boldsymbol{\epsilon}})I - \frac{P}{2}I, \quad P = \frac{P_0 \Delta}{2(\Delta + \Delta_{\min})}, \tag{5}$$

where the superscript T in Equation 4 indicates the transpose, I is the identity matrix and P is the replacement pressure, which has been introduced by Hibler and Ip (1995) to avoid divergence of ice in the absence of forces. The viscosities ζ, η are given by

$$\zeta = \frac{P_0}{2\left(\Delta^2 + \Delta_{\min}^2\right)^{\frac{1}{2}}}, \qquad \eta = e^{-2}\zeta, \qquad P_0(H, A) = P^\star H \exp(-C(1-A)), \tag{6}$$

where $e = 2$ is the ratio of the elliptic yield curve, $P^\star = 27{,}500$ N/m^2 is the ice strength parameter and $C = 20$. The parameter $\Delta_{\min} = 2 \times 10^{-9}$ is the viscous limit of the plastic regime, and

$$\Delta^2 = \left(\dot{\epsilon}_{11}^2 + \dot{\epsilon}_{22}^2\right)\left(1 + e^{-2}\right) + 4\dot{\epsilon}_{12}^2 e^{-2} + 2\dot{\epsilon}_{11}\dot{\epsilon}_{22}\left(1 - e^{-2}\right). \tag{7}$$

The elastic-viscous-plastic (EVP) formulation (Hunke & Dukowicz, 1997) has been introduced to regularize the VP rheology.

$$\partial_t \boldsymbol{\sigma} + \frac{e^2}{2T_{evp}}\boldsymbol{\sigma} + \frac{1-e^2}{4T_{evp}}\mathrm{tr}(\boldsymbol{\sigma})I + \frac{P}{4T_{evp}}I = \frac{\zeta}{T_{evp}}\dot{\epsilon}, \tag{8}$$

where $\mathrm{tr}(\cdot)$ denotes the trace and T_{evp} is the relaxation time that determines the transition time from the elastic regime to the VP rheology. The VP material law is recovered for $\partial_t \boldsymbol{\sigma} = 0$.

The most common approach to solve the coupled sea-ice system (Equations 1–3) is to split the equations in time. First, the approximation of the sea-ice momentum Equation 1 is computed, followed by solving the transport Equations 2 and 3. Due to stability concerns, fully explicit time stepping methods for the momentum equation are avoided as an extremely small time step is necessary in this case (Hibler & Schulson, 2000). There are currently two ways to address this issue. One of them relies on using an implicit time discretization and iterative methods such as Picard solvers (Ip et al., 1991; Lemieux & Tremblay, 2009) and Newton methods (Lemieux et al., 2010; Losch et al., 2014; Mehlmann & Richter, 2017; Shih et al., 2023). The other one still uses an explicit discretization, but relies on the EVP model, in which the artificial elastic term $\partial_t \boldsymbol{\sigma}$ in Equation 8 is added to the VP rheology, allowing for an explicit discretization of the momentum equation with relatively large time steps. In the EVP formulation of Hunke and Dukowicz (1997) numerical stability needs to be ensured by taking a sufficiently high number of subcycles. By slightly modifying the parameter choice of the EVP setup, stable solutions can be produced with reduced iteration count (Danilov et al., 2021). The original EVP model does not simulate the same deformation as VP models (Bouillon et al., 2013; Lemieux et al., 2012).

Recently, a modified version of the EVP method was developed, referred to as the mEVP solver, to ensure convergence to the solution of the VP model (Bouillon et al., 2013; Kimmritz et al., 2015; Lemieux et al., 2012). The mEVP method is designed in such a way that numerical stability and convergence are addressed separately. Considering the benchmark problem in Mehlmann et al. (2021b) where multiple LKFs are formed, Danilov et al. (2021) showed that EVP and mEVP methods lead to qualitative similar approximations if a sufficiently high number of subcycles is used. Using coarse meshes (27 km resolution) Kimmritz et al. (2017) showed that VP and mEVP approximations lead to quantitatively similar results in a realistic Arctic setup. Here, we demonstrate that this is also true for VP and EVP setups at high spatial resolution, see Section 4.3.

3. Methods

We consider the benchmark problem introduced by Mehlmann et al. (2021b), where a domain of size 512 km × 512 km is covered with a thin layer of sea ice, with an initial concentration of 100% and an initial thickness of approximately 0.3 m. A cyclone moves diagonally through the domain. During the two simulated days, multiple LKFs are formed.

3.1. Choice of Grids

Using the aforementioned benchmark problem, we evaluate the two CD-grid discretizations on both structured quadrilateral grids and unstructured meshes. On quadrilateral meshes, the CD-grid approaches are compared to approximations with a B-grid placement (CICE, Gascoigne) or a C-grid staggering (MITgcm). In the case of

triangular and hexagonal meshes, we compare the CD-grids to simulations with an A-grid placement (FESOM) or B-grid staggering (MPAS). A visualization of the setups considered in this manuscript is given in Figure 1. The different placements are summarized in Table 1.

In the quadrilateral case, we analyze the benchmark problem on grids with 8, 4, and 2 km cell side, which correspond to 4,096, 16,384, and 65,536 cells, respectively. Letting N be the number of cells, the CD-grid has $\frac{8N}{2}$ dof (degrees of freedom) whereas the B-grid has $\frac{8N}{4}$ dof. These number of dof have been obtained as follows. We have eight velocity components per cell; this amount is divided by two in the CD-grid setup, as two neighboring cells share a dof. In the B-grid case, a dof connects four adjacent cells. On triangular grids we use meshes with cells having a side length of 8, 4 and 2 km with 9,490, 37,926, 151,630 cells, respectively. The triangular CD-grid has $\frac{6N}{2}$ dof, and the B-grid has 2N dof. The runs on regular hexagonal grids are performed on meshes with a distance between hexagon centers of 8, 4 and 2 km. These meshes are made out of 4,464, 18,396, 74,676 cells, respectively. The hexagonal B-grids and CD-grids have 12N/3 dof and 12N/2 dof. A summary of the number of cells and the dof related to the placement of the variables is reported in Table 1.

3.2. Metrics

To compare the performance of different models, we consider the shear deformation

$$\dot{\epsilon}_{\text{shear}} = \sqrt{(\dot{\epsilon}_{11} - \dot{\epsilon}_{22})^2 + 4\dot{\epsilon}_{12}^2}, \tag{9}$$

simulated by the different model setups after 2 days. The shear deformation is analyzed either visually or by using an LKFs detection algorithm outlined by Hutter et al. (2019). The configuration of the algorithm used here interpolates the model data on a 2 km regular grid and detects LKFs by using image recognition tools in Python. After detection, the number and total length of LKFs are provided. The detection algorithm only identifies LKFs that are wider than one pixel to avoid the detection of noise. More details on configuration of the detection algorithm can be found in Mehlmann et al. (2021b).

We will compare the simulations in terms of two aspects. The amount of deformation with respect to the mesh size and the resolved structure in terms of dof. The simulated deformation with respect to the mesh is given by the total number or total length of LKFs for a given grid resolution. This metric highlights which discretization resolves more deformation structure on a fixed mesh. The second metric, the resolved structure per dof, is given by the number or length of LKFs for a given number of dof. This measure qualitatively characterizes the numerical effort used for the simulation of LKFs.

3.3. Model Configuration

We use the MPAS-Seaice model in the B-grid (Turner et al., 2021) and CD-grid (Capodaglio et al., 2023) configurations on quadrilateral and hexagonal meshes. In both setups, PWL basis functions (Bailey et al., 2008) are adopted for the computation of the divergence of the stress in the momentum Equation 1. The sea-ice drift is calculated based on the EVP method using 500 subcycles. As suggested by Danilov et al. (2022) we select $T_{evp} = 25$ min in the EVP algorithm. Please note that by increasing T_{evp} it will be possible to further decrease the number of subcycles. For the advection, an incremental remapping scheme is used (Turner et al., 2021). Due to the current lack of an incremental remapping scheme for a CD-grid, in such a case the velocities are first interpolated from the edges to the vertices and then the incremental remapping scheme as in the B-grid discretization is applied.

We compare the MPAS EVP approximations to simulations conducted with implicit solvers (CICE, Gascoigne, MITgcm) or the mEVP method (FESOM, ICON). In the case of the mEVP approximation, we apply 100 subcycles per time step. As in the setup of Mehlmann et al. (2021b) we solve the benchmark problem with a 2 min time step. Further details on the different model configurations can be found in Mehlmann et al. (2021b), whereas a description of the CD2 setup in FESOM is provided by Danilov et al. (2023a). Again, we refer to Table 1 for a summary of the discretization details.

4. Numerical Evaluation

In this section, we evaluate the ability of the CD1 and CD2 discretizations to reproduce LKFs. The analysis is conducted on structured and unstructured meshes and will proceed as follows. We start by analyzing the performance of the CD2 setup on triangular meshes in FESOM (Section 4.1). There, we consider an A-grid type as well as

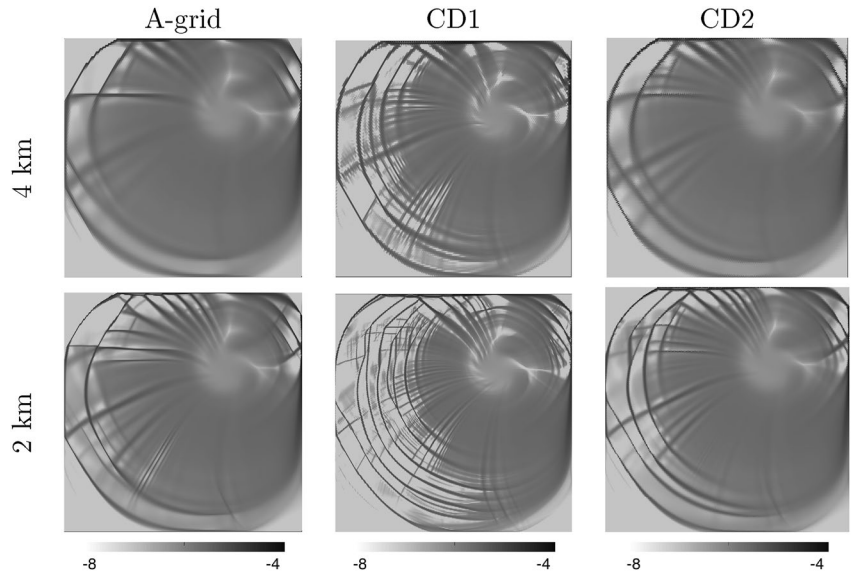

Figure 2. Shear deformation on a triangular mesh in FESOM. The shear deformation is given in s^{-1} and plotted in logarithmic scale.

a CD1 and CD2 discretization. Subsequently, the CD2 approach is analyzed on hexagonal meshes in the framework of MPAS (Section 4.2). The evaluation includes a comparison of the MPAS B-grid and CD-grid type discretization on meshes with the same dof. The B-grid configuration is obtained by increasing the number of cells by a factor of 1.5. Section 4.2 ends with a comparison of the CD2 discretization on triangular and hexagonal meshes. For this purpose, grids with approximately the same amount of dof are used. In Section 4.3, we evaluate the CD2 approach on quadrilateral mesh. As in the hexagonal case, the evaluation includes a comparison of the MPAS CD-grid and B-grid on meshes with the same dof. For this purpose, the number of cells are doubled in the B-grid case.

4.1. Triangular Meshes

The CD1 and CD2 discretizations are first compared using FESOM. Both setups place the velocity at the edge midpoint, use an upwind scheme to discretize (Equations 2 and 3), and the iterative mEVP method to solve the momentum Equation 1, see Table 1 for schematics.

Figure 2 presents the simulated shear deformation of the two CD-grid approaches. The corresponding number of detected LKFs and their total length are given in Figure 3. We attribute the significant changes in the simulated deformation to the spatial discretization, since this is the only place where the CD1 and CD2 approaches differ. The largest number of LKFs is generally simulated with the CD1 setup, followed by the CD2 approximation, and finally the A-grid discretization. This observation is confirmed by the LKF detection algorithm. Overall, the CD1 approach simulates finer structure than the CD2 and A-grid setup.

4.2. Hexagonal Meshes

We begin with analyzing the CD2 approach in MPAS. The CD-grid discretization and B-grid approach in MPAS only differ by the placement of the velocities and corresponding spatial discretization, see Table 1. Figure 4 shows that the MPAS CD2 discretization produces more structure than the B-grid setup. This is also reflected in the detected number and total length of LKFs presented in Figure 3. By comparing the B-grid and the CD-grid approach on meshes with the same number of dof, we see that the CD-grid setup still produces more structure than the B-grid approximation. This finding is supported by the result of detection algorithm presented in Figure 5.

In a second step, we compare the CD-grid approaches on hexagonal and triangular meshes. The MPAS CD2 implementation of the benchmark problem differs from the FESOM CD2 approximation by the choice of grid decomposition, the numerical realization of the subgrid discretization, the used pseudo time-stepping (mEVP vs. EVP) and the advection scheme, see Table 1 for a visual summary. To compare result of CD-grids on hexagonal

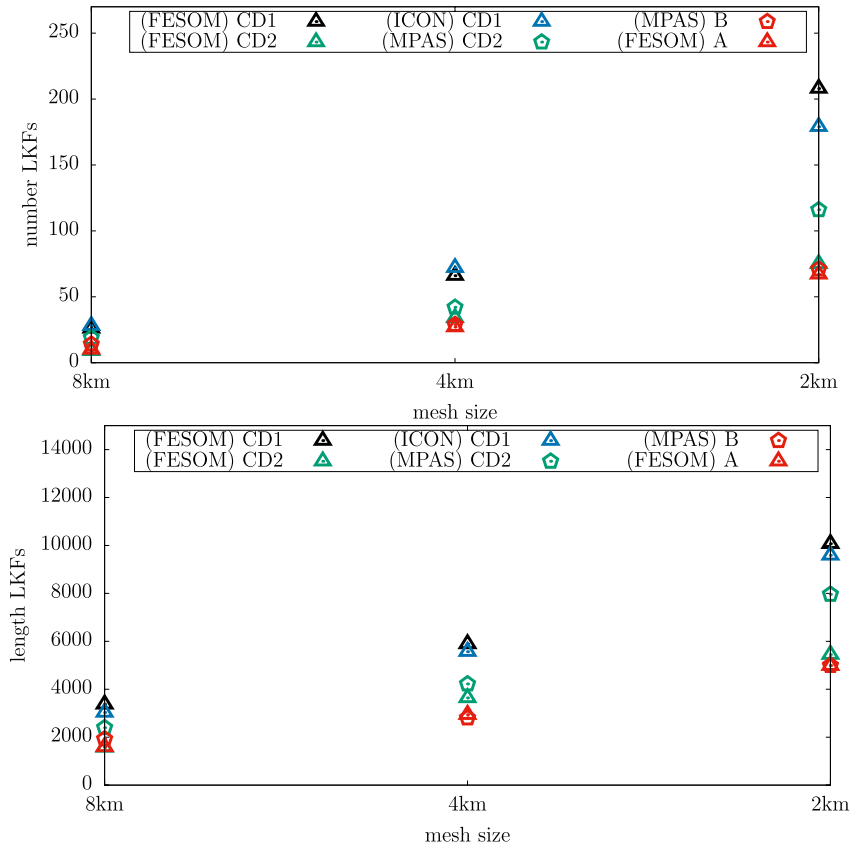

Figure 3. Total length and number of local kinematic features detected on triangular and hexagonal grids. Note that the CD-grid approaches have the same dof on hexagonal and triangular grids. The labels CD1 and CD2 refer to the CD-grid placements, whereas A, and B indicate an A-grid and B-grid staggering, respectively.

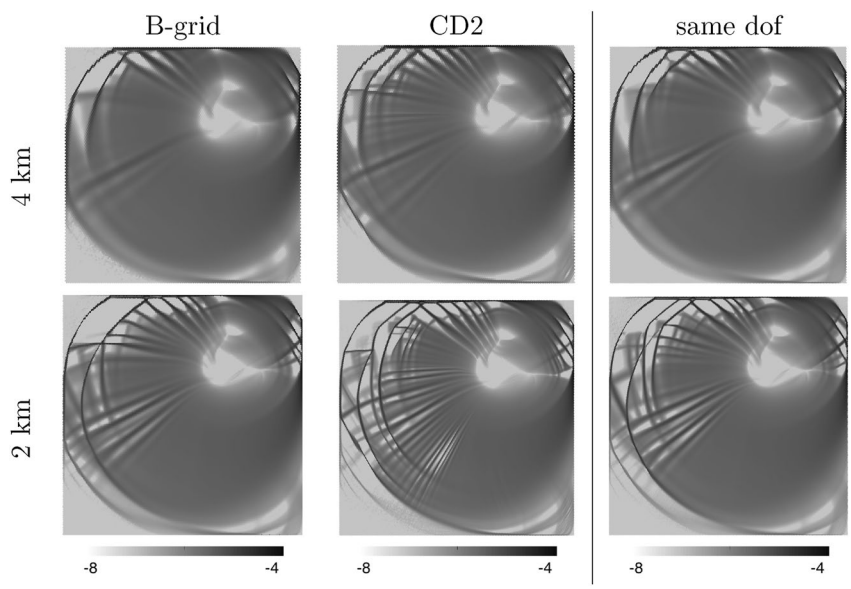

Figure 4. Shear deformation calculated on a hexagonal mesh using the MPAS framework. The third column presents the results preformed with a B-grid discretization on meshes that have the same velocity dof as the CD-grid. The shear deformation is given in s^{-1} and plotted in logarithmic scale.

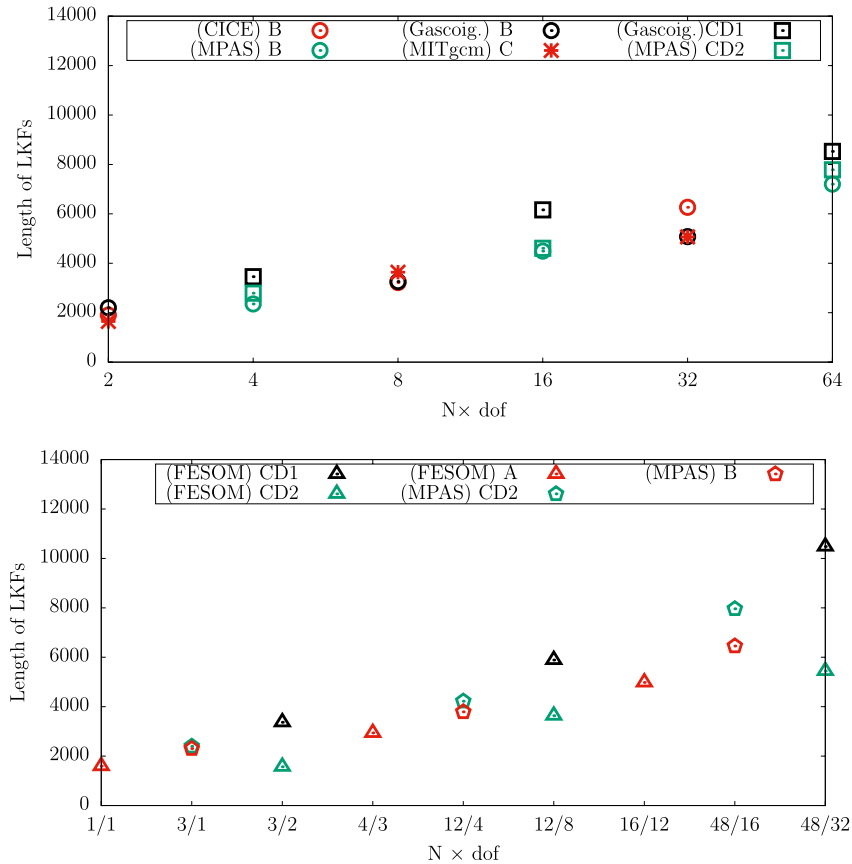

Figure 5. Detected number and total length of linear kinematic features with respect to the degrees of freedom (dof). N is the number of cells of the 8 km mesh. In the quadrilateral case (upper row) the numbers refer to the velocity dof. Note that all considered quadrilateral setups have the same tracer dof. In the triangular/hexagonal setup (bottom row) the numbers indicate the dof in the velocity/tracer components. The labels CD1 and CD2 refer to a CD-grid placement, whereas A, B, and C indicates an A-grid, B-grid, and C-grid staggering.

and triangular meshes, we use grids with the same dof (we refer to Section 3.1 for details on the mesh choice). The CD2 version in MPAS simulates less structure than the CD1 setup on triangular meshes. However it reproduces more deformation structure than the CD2 case on triangles (see Figure 4). This observation is also reflected in the output of the detection algorithm presented in Figure 3. This difference is likely due to the different implementations of the CD2 discretization in MPAS and FESOM.

4.3. Quadrilateral Meshes

In this section we consider simulations performed with MPAS and Gascoigne on quadrilateral meshes. While Gascoigne solves the VP equations implicitly, MPAS uses the EVP method. We start with pointing out that differences in the solver choice are minor compared to the effect of velocity placement. For this purpose, we present simulations based on a B-grid approximation that only differs in the chosen iterative method (see Figure 7). All three approach give qualitatively similar results. This can be further seen by comparing the shear deformation simulated with CD1 (Figure 6) to shear deformation presented in Figure 7 or by analyzing the amount of detected features in Figure 8.

The MPAS CD2 setup differs from the MPAS B-grid discretization only by the placement of the velocity degrees of freedom and the associated spatial discretization. In contrast, the MPAS CD2 discretization and the CD1 approach in Gascoigne have the same placement of the velocity and the tracer points. Therefore CD1 and CD2 have the same number of dof. Apart from that, the two setups differ by the used numerical methods to discretize the equations, see Table 1.

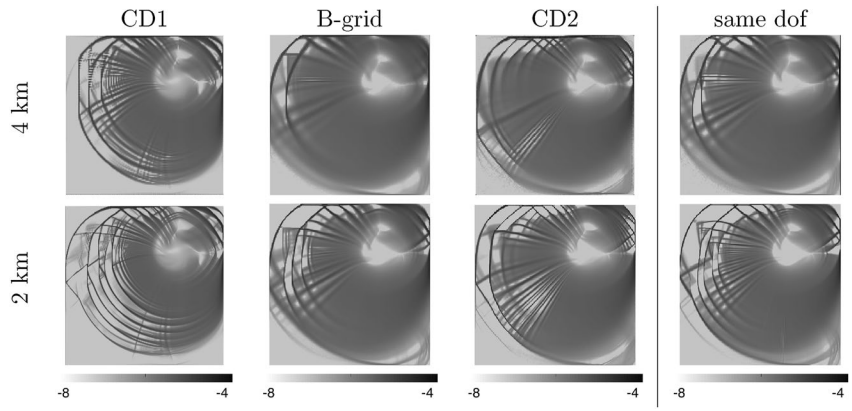

Figure 6. Shear deformation on quadrilateral meshes. The CD1 simulation is performed in Gascoigne whereas the CD2 and B-grid runs are carried out in the framework of MPAS. The fourth column "same dof" refers to a B-grid discretization with the same velocity dof as the CD-grids on 4 km or 2 km. The shear deformation is given in s^{-1} and plotted in logarithmic scale.

The CD1 and CD2 approximation resolve more structure with respect to the cell size than the corresponding B-grid approach in MPAS and Gascoigne, see Figure 6 (column 1–3). Figure 6 shows that the CD2 setup simulates less structure than the CD1 approach. This observations are confirmed by the results of the detection algorithm presented in Figure 8.

5. Discussion

Due to uncertainties in the detection algorithm (Mehlmann et al., 2021b) we discuss only results that exhibit a consistent trend across all three measures - the number of LKFs, the length of LKFs, and visual evaluation of the approximation.

The numerical analysis in Section 4 shows that, among the discretizations considered, here the CD-grids resolve more LKFs for given grid resolution than the A-grid on triangular meshes, the hexagonal B-grid and the quadrilateral B-grid/C-grid. This can mainly be attributed to the fact that the CD-grids double the dof on quadrilateral grids, triples the dof on triangular meshes compared to A-grids and increase the dof by factor 1.5 compared to hexagonal B-grids. Overall the nonconforming CD1 approximation produces more deformation structure for

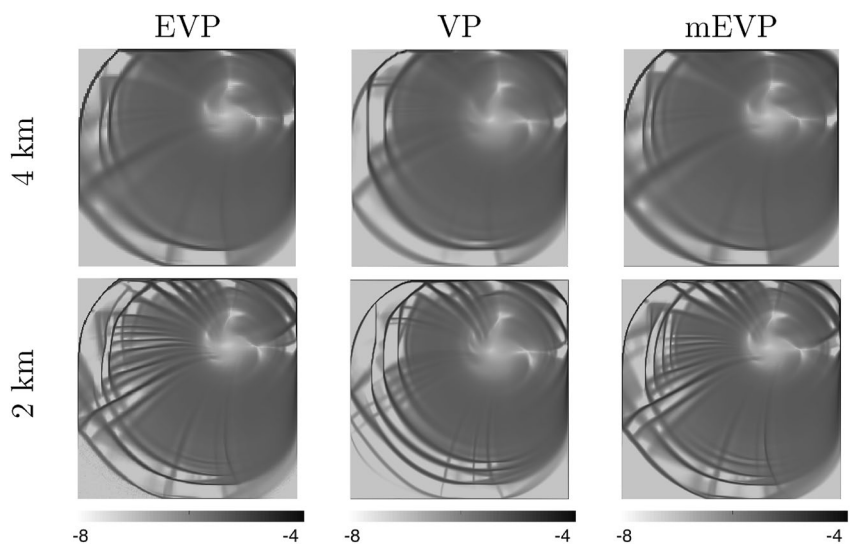

Figure 7. B-grid that only differs by the (m) (E)VP formulation. The shear deformation is given in s^{-1} and plotted in logarithmic scale.

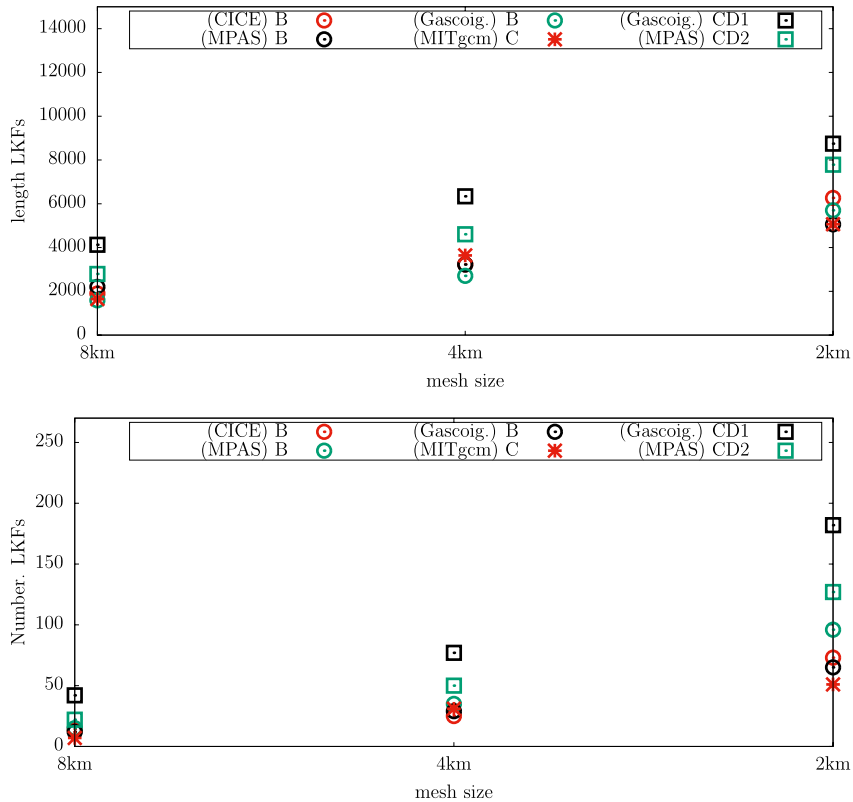

Figure 8. Detected length and number of linear kinematic features on quadrilateral grids with a side length of 8, 4 and 2 km. The label CD1 and CD2 refer to a CD-grid placement, whereas B and C indicates a B-grid and C-grid staggering.

given grid resolution than the CD2 setup on both quadrilateral and hexagonal/triangular meshes, even though the CD1 and CD2 approximation have the same number of dof. The nonconforming CD1 approach resolves more LKFs than quadrilateral B-grids/C-grids and triangular A-grids but on meshes with doubled grid spacing (less dof), see Figure 5. This conclusion can not be drawn for the CD2 setup (see Figure 5). The CD2 approximation does not provide the same accuracy per dof neither on quadrilateral nor on triangular/hexagonal meshes.

The lower production of LKFs in the CD2 setup can be explained as follows. In the quadrilateral case the CD2 approach can be interpreted as a rotated B-grid with a doubled number of cells. For simplicity we consider a unit square with $N = \frac{1}{h^2}$ cells. The rotated B-grid can be viewed as a diamond shaped element that is placed in each quadrilateral cell. The side length of the diamond is given by $\frac{h}{\sqrt{2}}$. This means that in case of the rotated grid the number of elements rise to $2N = \frac{2}{h^2}$. Therefore the rotated B-grid has the same accuracy as the B-grid on meshes with a side length of $h\sqrt{2}$ that is, $\frac{N}{2}$ cells. The CD1 approach simulates the same deformation structure as the B-grid but on meshes twice as coarse (Mehlmann et al., 2021b). Thus the CD1 grid has the same accuracy as the B-grid on meshes with a grid spacing of $2h$ that is, $\frac{N}{4}$. This shows that CD1 approach simulates more structure w.r.t. the mesh size than the CD2 discretization and the B-grid simulates less LKFs than the CD2 framework.

When comparing the performance of the new CD2 approximation to traditional discretizations, we observed that on hexagonal grids with the same dof in the velocity the CD2 simulates more LKFs than the B-grid (see Figure 5). This result could not be confirmed on quadrilateral meshes (see Figure upper plot 5). We attribute such a different behavior on quadrilateral and hexagonal meshes to the different ratio of velocity and tracer dof. Note that the comparison on grids with the same number of dof is slightly in favor of the B-grid because doubling the number of cells also doubles the dof of the tracers. It has been shown by Mehlmann and Danilov (2022) that more dof in the tracer point promotes the production of LKFs as the thickness and concentration influences the representation of the pressure P in the rheology (2).

In case of the benchmark problem, implicit solving VP and explicit subcyling (m)EVP leads to qualitatively similar results (see Figure 7). We conclude that the differences in the simulation of LKFs introduced by varying

the solvers are much smaller than differences between CD1 and CD2 grids. We observe that the CD1 discretization needs the configuration of a stabilization parameter, which in case of implicit solvers has been identified (Mehlmann & Korn, 2021; Mehlmann et al., 2021b), while the optimal choice in the context of (m)EVP methods requires additional tuning. The CD2 setup on the other hand does not need additional stabilization, which is an advantage of such approach. The need of a stabilization in CD1 or the subgrid discretization of the strain rates in the CD2 approach increases the computational time. A comparison on triangular grids in the framework of FESOM shows that the CD-grid discretizations increase the computational time roughly by factor 2 (CD1) or factor 4 (CD2) compared to the A-grid, see (Danilov et al., 2023a). The A-grid discretization resolves a similar structure as the CD1 setup on meshes with half of the grid spacing which increases the computational cost of the A-grid approximation by factor 4.

(E)VP models show an improved agreement to observational data with increasing mesh resolution, by simulating multiple LKFs (Bouchat et al., 2022; Hutter et al., 2022). In this sense the benchmark problem is used to address the question of whether more elaborate discretizations can simulate more deformation structure. An increased number of LKFs is just one indicator for an increased accuracy. The Fourier analysis in Danilov et al. (2022, 2023a) has demonstrated that the CD1 approximation provides the greatest accuracy, followed by the CD2 approximation, and the A-grid. It remains to be shown for the CD-grids that the simulated deformations reproduces observed scaling characteristics in Pan Arctic sea-ice simulations. In this perspective it would be interesting to compare the nonconforming CD1 setup to the results presented in the SIRex project (Bouchat et al., 2022; Hutter et al., 2022). As main deformation characteristics are present in all the considered discretizations (see Figures 2, 4, and 6), it is likely that the discussed setups will simulate observed scaling characteristics to a certain extent.

The number of dof for a given grid spacing is a key parameter for the simulation of LKFs. Our analysis considers low order approximations. For the benchmark problem considered here, a second order conforming finite element discretization has been tested by Shih et al. (2023). The discretization showed higher resolving capacity than the first order conforming finite element approximation. It would be of interested to compare the performance of high order spatial discretizations to the presented CD-grids.

6. Conclusion

We find that the nonconforming CD1 approximation (Mehlmann & Korn, 2021; Mehlmann et al., 2021b) produces more deformation structure than the CD2 approach (Capodaglio et al., 2023) on both quadrilateral and triangular meshes, even though both CD-grids have the same number of dof. This shows that besides the placement of the velocity, the chosen spatial discretization plays an important role for the simulation of LKFs.

The nonconforming CD1 approach provides a promising resolution property. Even though CD-grids doubles the number of dof compared to quadrilateral A, B, and C-grids and triples the dof of the triangular A-grid, the CD1 setup simulates qualitatively similar LKFs on meshes with half of the grid spacing (4 times less dof). We found that the CD2 setup does not have this resolution capacity. However on hexagonal meshes with the same number of dof the MPAS CD2 approach simulates more LKFs than the MPAS B-grid setup.

The CD-grid discretizations resolve more LKFs than standard A, B, or C-grids on a fixed mesh. This can mainly be attributed to the higher number of velocity dof, which is an appealing property as for the simulation of deformation structure in VP sea-ice models a high spatial mesh resolution is needed.

Data Availability Statement

The version of MPAS-Seaice used for the results in this paper is provided at https://doi.org/10.5281/zenodo.7662610 (Edwards et al., 2023). The sea-ice component of FESOM used for simulations reported here is available at https://doi.org/10.5281/zenodo.7646908 (Danilov et al., 2023b). The Gascoigne, ICON, MITgcm, CICE, FESOM (A-grid and CD1) data is available at (Mehlmann et al., 2021a). The MPAS and FESOM CD2 data and the routines to process it can be accessed via https://data.mendeley.com/datasets/7h9hkjvx48/1 (Mehlmann et al., 2023).

Acknowledgments
We thank N. Hutter for the development of his LKF diagnostics methodology. C. Mehlmann is funded by the Deutsche Forschungsgemeinschaft (DFG, German Research Foundation)—Project number 463061012. Document approved for unlimited release: LA-UR-23-21941. This paper is a contribution to the project S2: Improved parameterizations and numerics in climate models of the Collaborative Research Centre TRR 181 "Energy Transfer in Atmosphere and Ocean" funded by the Deutsche Forschungsgemeinschaft (DFG, German Research Foundation)—project no. 274762653. Open Access funding enabled and organized by Projekt DEAL.

References

Bailey, T. S., Adams, M. L., Yang, B., & Zika, M. R. (2008). A piecewise linear finite element discretization of the diffusion equation for arbitrary polyhedral grids. *Journal of Computational Physics*, *227*(8), 3738–3757. https://doi.org/10.1016/j.jcp.2007.11.026

Becker, R., Braack, M., Meidner, D., Richter, T., & Vexler, B. (2019). The finite element toolkit Gascoigne [Computer software manual]. http://www.uni-kiel.de/gascoigne/

Blockley, E., Vancoppenolle, M., Hunke, E., Bitz, C., Feltham, D., Lemieux, J.-F., et al. (2020). The future of sea ice modeling: Where do we go from here? *Bulletin of the American Meteorological Society*, *101*(8), 1304–1311. https://doi.org/10.1175/BAMS-D-20-0073.1

Bouchat, A., Hutter, N., Chanut, J., Dupont, F., Dukhovskoy, D., Garric, G., et al. (2022). Sea Ice Rheology Experiment (SIREx): 1. Scaling and statistical properties of sea-ice deformation fields. *Journal of Geophysical Research: Oceans*, *127*(4), e2021JC017667. https://doi.org/10.1029/2021JC017667

Bouchat, A., & Tremblay, B. (2017). Using sea-ice deformation fields to constrain the mechanical strength parameters of geophysical sea ice. *Journal of Geophysical Research: Oceans*, *122*(7), 5802–5825. https://doi.org/10.1002/2017JC013020

Bouillon, S., Fichefet, T., Legat, V., & Madec, G. (2013). The elastic-viscous-plastic method revisited. *Ocean Modelling*, *71*, 2–12. https://doi.org/10.1016/j.ocemod.2013.05.013

Capodaglio, G., Petersen, M. R., Turner, A. K., & Roberts, A. F. (2023). An unstructured CD-grid variational formulation for sea ice dynamics. *Journal of Computational Physics*, *473*, 111742. https://doi.org/10.1016/j.jcp.2022.111742

Coon, M., Kwok, R., Levy, G., Pruis, M., Schreyer, H., & Sulsky, D. (2007). Arctic Ice Dynamics Joint Experiment (AIDJEX) assumptions revisited and found inadequate. *Journal of Geophysical Research*, *112*(C11), C11S90. https://doi.org/10.1029/2005jc003393

Danilov, S., Koldunov, N., Sidorenko, D., Scholz, P., & Wang, Q. (2021). On the damping time scale of EVP sea ice dynamics. *Journal of Advances in Modeling Earth Systems*, *13*(10), e2021MS002561. https://doi.org/10.1029/2021MS002561

Danilov, S., Mehlmann, C., & Fofonova, V. (2022). On discretizing sea-ice dynamics on triangular meshes using vertex, cell or edge velocities. *Ocean Modelling*, *170*, 101937. https://doi.org/10.1016/j.ocemod.2021.101937

Danilov, S., Mehlmann, C., Sidorenko, D., & Wang, Q. (2023a). CD-type discretization for sea ice dynamics in FESOM version 2. *Geoscientific Model Development Discussions*, 1–17. https://doi.org/10.5194/gmd-2023-37

Danilov, S., Mehlmann, C., Sidorenko, D., & Wang, Q. (2023b). Sea ice CD-type discretizations of FESOM [Software]. Zenodo. https://doi.org/10.5281/zenodo.7646908

Danilov, S., Wang, Q., Timmermann, R., Iakovlev, N., Sidorenko, D., Kimmritz, M., et al. (2015). Finite-element sea ice model (FESIM), version 2. *Geoscientific Model Development*, *8*(6), 1747–1761. https://doi.org/10.5194/gmd-8-1747-2015

Dansereau, V., Weiss, J., Saramito, P., & Lattes, P. (2016). A Maxwell elasto-brittle rheology for sea ice modelling. *The Cryosphere*, *10*(3), 1339–1359. https://doi.org/10.5194/tc-10-1339-2016

Dasgupta, G. (2003). Interpolants within convex polygons: Wachspress' shape functions. *Journal of Aerospace Engineering*, *16*, 1–8. https://doi.org/10.1061/(ASCE)0893-1321(2003)16:1(1)

Edwards, J., Foucar, J., Petersen, M., Hoffman, M., Jacobsen, D., Duda, M., et al. (2023). gcapodag/E3SM: CD-grid MPAS-Seaice E3SM source code for LKFs paper runs (Dec2022). (CD-grid_LKFs_Dec2022) [Software]. Zenodo. https://doi.org/10.5281/zenodo.7662610

Feltham, D. L. (2008). Sea ice rheology. *Annual Review of Fluid Mechanics*, *40*(1), 91–112. https://doi.org/10.1146/annurev.fluid.40.111406.102151

Hibler, W. D. (1979). A dynamic thermodynamic sea ice model. *Journal of Physical Oceanography*, *9*(4), 815–846. https://doi.org/10.1175/1520-0485(1979)009<0815:adtsim>2.0.co;2

Hibler, W. D., & Schulson, E. M. (2000). On modeling the anisotropic failure and flow of flawed sea ice. *Journal of Geophysical Research*, *105*(C7), 17105–17120. https://doi.org/10.1029/2000jc900045

Hibler, & Ip, C. F. (1995). The effect of sea ice rheology on Arctic buoy drift. In J. P. Dempsey & Y. D. S. Rajapakse (Eds.), *ASME AMD* (Vol. 207, pp. 255–263). Ice Mechanics.

Hunke, E., & Dukowicz, J. (1997). An elastic-viscous-plastic model for sea ice dynamics. *Journal of Physical Oceanography*, *27*(9), 1849–1867. https://doi.org/10.1175/1520-0485(1997)027<1849:aevpmf>2.0.co;2

Hunke, E., Lipscomb, W., Turner, A., Jeffery, N., & Elliott, S. (2015). CICE: The Los Alamos Sea Ice Model documentation and software user's manual version 5.1 la-cc-06-012 [Computer software manual]. https://csdms.colorado.edu/w/images/CICE_documentation_and_software_user's_manual.pdf

Hutchings, J., Heil, P., & Hibler, W. (2005). Modeling linear kinematic features in sea ice. *Monthly Weather Review*, *133*(12), 3481–3497. https://doi.org/10.1175/mwr3045.1

Hutter, N., Bouchat, A., Dupont, F., Dukhovskoy, D., Koldunov, N., Lee, Y. J., et al. (2022). Sea Ice Rheology Experiment (SIRex): 2. Evaluating linear kinematic features in high-resolution sea ice simulations. *Journal of Geophysical Research: Oceans*, *127*(4), e2021JC017666. https://doi.org/10.1029/2021JC017666

Hutter, N., & Losch, M. (2020). Feature-based comparison of sea ice deformation in lead-permitting sea ice simulations. *The Cryosphere*, *14*(1), 93–113. https://doi.org/10.5194/tc-14-93-2020

Hutter, N., Zampieri, L., & Losch, M. (2019). Leads and ridges in Arctic sea ice from RGPS data and a new tracking algorithm. *The Cryosphere*, *13*(2), 627–645. https://doi.org/10.5194/tc-13-627-2019

Ip, C., Hibler, W., & Flato, G. (1991). On the effect of rheology on seasonal sea-ice simulations. *Annals of Glaciology*, *15*, 17–25. https://doi.org/10.3189/1991aog15-1-17-25

Kimmritz, M., Danilov, S., & Losch, M. (2015). On the convergence of the modified elastic-viscous-plastic method for solving the sea ice momentum equation. *Journal of Computational Physics*, *296*, 90–100. https://doi.org/10.1016/j.jcp.2015.04.051

Kimmritz, M., Losch, M., & Danilov, S. (2017). A comparison of viscous-plastic sea ice solvers with and without replacement pressure. *Ocean Modelling*, *115*, 59–69. https://doi.org/10.1016/j.ocemod.2017.05.006

Koldunov, N., Danilov, S., Sidorenko, D., Hutter, N., Losch, M., Goessling, H., et al. (2019). Fast EVP solutions in a high-resolution sea ice model. *Journal of Advances in Modeling Earth Systems*, *11*(5), 1269–1284. https://doi.org/10.1029/2018MS001485

Kwok, R. (2001). Deformation of the Arctic Ocean sea ice cover between November 1996 and April 1997: A qualitative survey. In *IUTAM Symposium on Scaling Laws in Ice Mechanics and Ice Dynamics* (pp. 315–322). Springer Netherlands.

Lemieux, J., Knoll, D., Tremblay, B., Holland, D., & Losch, M. (2012). A comparison of the Jacobian-free Newton-Krylov method and the EVP model for solving the sea ice momentum equation with a viscous-plastic formulation: A serial algorithm study. *Journal of Computational Physics*, *231*(17), 5926–5944. https://doi.org/10.1016/j.jcp.2012.05.024

Lemieux, J., & Tremblay, B. (2009). Numerical convergence of viscous-plastic sea ice models. *Journal of Geophysical Research*, *114*(C5), C05009. https://doi.org/10.1029/2008JC005017

Lemieux, J., Tremblay, B., Sedláček, J., Tupper, P., Thomas, S., Huard, D., & Auclair, J. (2010). Improving the numerical convergence of viscous-plastic sea ice models with the Jacobian-free Newton-Krylov method. *Journal of Computational Physics*, *229*(8), 2840–2852. https://doi.org/10.1016/j.jcp.2009.12.011

Losch, M., Fuchs, A., Lemieux, J., & Vanselow, A. (2014). A parallel Jacobian-free Newton-Krylov solver for a coupled sea ice-ocean model. *Journal of Computational Physics*, *257*, 901–911. https://doi.org/10.1016/j.jcp.2013.09.026

Losch, M., Menemenlis, D., Campin, J.-M., Heimbach, P., & Hill, C. (2010). On the formulation of sea-ice models. Part 1: Effects of different solver implementations and parameterizations. *Ocean Modelling*, *33*(1), 129–144. https://doi.org/10.1016/j.ocemod.2009.12.008

Mehlmann, C., & Danilov, S. (2022). The effect of the tracer staggering on sea ice deformation fields. *CIMNE*. https://doi.org/10.23967/eccomas.2022.267

Mehlmann, C., Danilov, S., & Capodaglio, G. (2023). Numerical evaluation of CD-type discretizations of sea-ice dynamics. (Version 1) [Dataset]. Mendeley Data. https://doi.org/10.17632/7h9hkjvx48.1

Mehlmann, C., Danilov, S., Losch, M., Lemieux, J.-F., Hutter, N., Richter, T., et al. (2021a). Sea ice numerical VP-comparison benchmark. (Version 1) [Dataset]. Mendeley Data. https://doi.org/10.17632/kj58y3sdtk.1

Mehlmann, C., Danilov, S., Losch, M., Lemieux, J. F., Hutter, N., Richter, T., et al. (2021b). Simulating linear kinematic features in viscous-plastic sea ice models on quadrilateral and triangular grids with different variable staggering. *Journal of Advances in Modeling Earth Systems*, *13*(11), e2021MS002523. https://doi.org/10.1029/2021ms002523

Mehlmann, C., & Korn, P. (2021). Sea-ice dynamics on triangular grids. *Journal of Computational Physics*, *428*, 110086. https://doi.org/10.1016/j.jcp.2020.110086

Mehlmann, C., & Richter, T. (2017). A modified global Newton solver for viscous-plastic sea ice models. *Ocean Modelling*, *116*, 96–107. https://doi.org/10.1016/j.ocemod.2017.06.001

Rampal, P., Bouillon, S., Olason, E., & Morlighem, M. (2016). neXtSIM: A new Lagrangian sea ice model. *The Cryosphere*, *10*(3), 1055–1073. https://doi.org/10.5194/tc-10-1055-2016

Rampal, P., Weiss, J., Marsan, D., Lindsay, R., & Stern, H. (2008). Scaling properties of sea ice deformation from buoy dispersion analysis. *Journal of Geophysical Research*, *113*(C3), C03002. https://doi.org/10.1029/2007JC004143

Shih, Y., Mehlmann, C., Losch, M., & Stadler, G. (2023). Robust and efficient primal-dual Newton-Krylov solvers for viscous-plastic sea-ice models. *Journal of Computational Physics*, *474*, 111802. https://doi.org/10.1016/j.jcp.2022.111802

Stroeve, J., & Notz, D. (2018). Changing state of Arctic sea ice across all seasons. *Environmental Research Letters*, *13*(10), 103001. https://doi.org/10.1088/1748-9326/aade56

Tsamados, M., Feltham, D. L., & Wilchinsky, A. V. (2013). Impact of a new anisotropic rheology on simulations of Arctic sea ice. *Journal of Geophysical Research: Oceans*, *118*(1), 91–107. https://doi.org/10.1029/2012jc007990

Turner, A. K., Lipscomb, W. H., Hunke, E. C., Jacobsen, D. W., Jeffery, N., Engwirda, D., et al. (2021). MPAS-Seaice (v1.0.0): Sea-ice dynamics on unstructured Voronoi meshes. *Geoscientific Model Development*, *15*(9), 3721–3751. https://doi.org/10.5194/gmd-2021-355

Wang, Q., Danilov, S., Jung, T., Kaleschke, L., & Wernecke, A. (2016). Sea ice leads in the Arctic Ocean: Model assessment, interannual variability and trends. *Geophysical Research Letters*, *43*(13), 7019–7027. https://doi.org/10.1002/2016GL068696